Journal of Power Sources 196 (2011) 1704–1711

Contents lists available at ScienceDirect

Journal of Power Sources

journal homepage: www.elsevier.com/locate/jpowsour

Effects of rapid process on the conductivity of multiple elements doped ceria-based electrolyte

Horng-Yi Chang[a,*], Yao-Ming Wang[a], Chia-Hsin Lin[b], Syh-Yuh Cheng[b]

[a] Department of Marine Engineering, National Taiwan Ocean University, 2 Pei-Ning Road, Keelung 20224, Taiwan, ROC
[b] Ceramic Microengineering Laboratory, Material and Chemical Research Laboratories, Industrial Technology Research Institute, Chutung 31060, Taiwan, ROC

ARTICLE INFO

Article history:
Received 13 August 2010
Received in revised form 12 October 2010
Accepted 14 October 2010
Available online 11 November 2010

Keywords:
Ceria
Ionic conductivity
Solid oxide fuel cell
Citric acid-based combustion technique
Microwave sintering

ABSTRACT

The citric acid-based combustion technique (SV) for powder preparation and the rapid microwave sintering (MW) process are used to lower the synthesizing temperature and to shorten the processing time then to modify the grain boundary resistance and oxygen vacancies mobility in multiple elements doped ceria-based electrolyte (LSBC). Nanoparticles of less than 50 nm with a pure fluorite structure are prepared by SV method at a low temperature of 600 °C. Microwave sintering lowers the sintering temperature to 1400 °C from the conventional sintering (CS) temperature of 1500 °C needed for solid-state (SS) prepared LSBC, and requires only 15 min of sintering time. The SV sample conventionally sintered at 1400 °C–6 h reaches a conductivity of 0.006 S cm^{-1}. When the SV samples are microwave sintered at 1400 °C–15 min, they achieve a conductivity as high as 0.01 S cm^{-1} measured at 600 °C. Microwave sintering reduces the grain boundary resistance of both SS and SV samples. The migration enthalpy (H_m) of 0.66 eV in the SS-MW and SV-MW samples is similar to that of the fully densified SS-CS sample. The Schottky barrier height can be adjusted by SV powder preparation and by the MW process using a slightly lower sintering temperature and with a shorter processing time for multiple elements doped solid electrolyte.

1. Introduction

The solid oxide fuel cell (SOFC) has the highest power conversion efficiency among fuel cells, and it can be used in a wide range of power conversion systems. The SOFC directly converts the chemical energy of the fuel into electric energy. Generally speaking, it operates in the range of 800–1000 °C for ZrO_2-based electrolyte [1]. Lowering the operating temperature below 800 °C (below 600 °C is even better) allows using fuels such as methane and butane without pre-forming. The benefits of a lower operating temperature include a wide selection of materials, long-term stability, interface matching of the cell system and a cost effective manufacturing and operation [2].

One significant bottle-neck in the development of an intermediate temperature solid oxide fuel cell (ITSOFC) is the low oxygen ionic conductivity of solid electrolyte at such a temperature, e.g., 600 °C. In addition to reducing the electrolyte thickness, achieving the ability to use a high ionic conductivity composition of electrolytes is an important goal for the ITSOFC. It is evident that the ionic conductivity can be improved for ceria doped with suitable aliovalent cationic dopants. Co-doping has been proven to effectively improve the electrical properties of ceria-based electrolytes [3]. Mori et al. studied a large strain in the lattice of doped ceria created by doping lower valent cations on the Ce site. In order to minimize the distortion in the lattice, micro-domains form spontaneously in the lattice. Mori et al. found Sm or La and alkaline earth co-doped ceria-based electrolytes with a high crystallographic (effective) index resulting in small micro-domains of around 1–3 nm in the microstructure. The multiple elements doped ceria-based electrolyte then improves the passing oxygen ions through the oxide lattice as a result of the size reduction of the oxygen vacancies ordering domains [4]. Thus, ceria materials co-doped with di- or tri-valent elements possess a high oxygen ionic conductivity with a potential use as an electrolyte at intermediate temperatures [5,6]. In order to expand and improve the ionic conductivity of multiple doped electrolyte, the most important areas of concern are processing methods, microstructural control of grain and grain boundary [7,8]. Once these concerns are addressed, the ionic conductivity can be improved by a change in the microstructure on an atomic scale. In addition, since electrical conduction is greatly dependent on the homogeneous concentration of doping elements [9], the preparation of the cerium oxide sample doped with rare earth/alkaline earth must consider the homogeneity of these doping atoms in the sample.

Thus, the key factors in the design of ceria-based electrolyte are the choice of dopants and the preparation method of the powder because they both very strongly influence the homogeneity and stability of the electrolyte solid solutions [10]. There are

* Corresponding author. Tel.: +886 2 24621292x7103; fax: +886 2 24633765.
E-mail address: hychang@mail.ntou.edu.tw (H.-Y. Chang).

0378-7753/$ – see front matter © 2010 Elsevier B.V. All rights reserved.
doi:10.1016/j.jpowsour.2010.10.035

several problems associated with the preparation of doped-ceria electrolytes. They are difficult to prepare at low calcination and sintering temperatures when using conventional mixed oxide powders [11,12]. For example, a pure phase, multiple elements doped ceria-based electrolyte, $(La_{0.75}Sr_{0.2}Ba_{0.05})_{0.175}Ce_{0.825}O_{1.891}$ (LSBC), is difficult to synthesize at a low calcination temperature (e.g., <600 °C). A high sintering temperature, e.g., >1500 °C, is also needed by the conventional solid-state reaction method [12,13] to obtain a pure fluorite structure and high density. These high sintering temperatures may lead to the reduction of Ce^{4+} to Ce^{3+} and accompany the formation of oxygen vacancies [14,15]. The tendency of oxygen vacancy formation retards densification and further lowers the mechanical stability of the material [16,17].

Upon homogenizing the dopant distribution, the average grain size of the crystallites and promoting the sintered density as well as maintaining the crystal phase one can expect an effective improvement of ionic conductivity of the solid electrolytes. The solid electrolytes possess a well-developed intercrystalline boundary, whose properties are likely to substantially affect the charge transport. As a result, the microstructures are strongly dependent on the powder preparation and the sintering process. In general, nanoparticles show a higher catalytic activity, better sinterability, better conductivity and other unusual properties contrary to that of bulk materials [18]. Lately, many chemical methods have been developed to synthesize ceria-based electrolyte nanoparticles, including precipitation [19], aerosol flame deposition [20,21], glycine–nitrate combustion [22], citric acid-based sol–gel process [23], laser evaporation [24], freeze-drying [25] and hydrothermal preparation [26] among others. The sintering temperature is substantially lowered by chemically synthesized powders and by the addition of sintering aids [15]. However, to obtain a pure phase multi-element doped LSBCs at low calcination temperature with dense homogeneous grains in a shorter processing time by rapid sintering using the conventional mixed oxide powder preparation and sintering methods remains difficult. Microwave sintering is a rapid sintering process providing both time and energy savings. Recently, YSZ-based SOFC [27], alumina/cerium oxide nano-composite electrolyte [28], dense LSGM electrolytes [29] and dense ceria and $Ce_{0.8}Gd_{0.2}O_{1.9}$ pellets [30] were prepared using either a domestic or an industrial microwave oven, showing the method to be cost-effective and time-saving.

The objective of this study was to investigate how the rapid microwave process modifies the grain boundary and the grain conduction behavior of multiple elements doped solid electrolyte. The synthesis of multiple element-doped electrolyte composition uses the conventional solid-state reaction (SS) method and then uses the low temperature citric acid-based combustion technique (SV) in order to obtain more active particles and homogeneous multiple-doped elements. Afterwards, the SV and SS prepared powders are subjected to conventional sintering (CS) to compare their ionic conductivities. Finally, the microwave sintering (MW) process is used to densify the SS- and SV-prepared powders in order to evaluate the modified microstructural grains and the effects of the grain boundaries on the conductivity of the electrolyte.

2. Experimental

The chemical composition of multiple elements doped solid electrolyte is $(La_{0.75}Sr_{0.2}Ba_{0.05})_{0.175}Ce_{0.825}O_{1.891}$ (LSBC). The following raw materials were utilized in the citric acid-based combustion technique: $La(NO_3)_3{\cdot}6H_2O$ (Merck, 97%), $Sr(NO_3)_2$ (Merck, 98%), $Ba(CH_3COO)_2$ (Showa, 99%) and $Ce(NO_3)_3{\cdot}6H_2O$ (Showa, 99%). The solid-state reaction method used La_2O_3 (Merck, 99.99%), $SrCO_3$ (Merck, 98%), $BaCO_3$ (Showa, 99%) and ceria (ACROS Organics, 99.9%) as the starting materials.

For the citric acid-based combustion technique (SV), La, Sr, Ba and Ce were first dissolved in de-ionized water. Citric acid was used as the chelating agent. The mixed aqueous solution had a molar ratio of 1:2 for LSBC:citric acid. This mixed solution was then heated on a hot-plate at 90 °C to evaporate the water content, which finally turned into a yellow gel. This gel was then oven-dried at about 100 °C. The dried gel was then pulverized and calcined at 600–900 °C–2 h. In the solid-state (SS) reaction method, the starting materials were mixed in a PE-bottle with yttrium-stabilized zirconia milling medium and de-ionized water, ball-milled for 12 h. The ball-milled slurry was then oven-dried at about 100 °C. The dried powders were then calcined at 900–1100 °C–2 h.

Both of the calcined powders (SS and SV powders) were then further milled using a mortar and pestle and were then granulated with a binder. The granulated powders were then pressed in a die using a uniaxial press to form a disk measuring 10 mm diameter × 1 mm thick. The pressed disks were then subjected to conventional sintering (CS) in an electrical furnace at 1300–1500 °C–6 h. Rapid sintering was carried out in a focused microwave cavity [31] at different power settings and duration.

The crystal structures of the prepared powders and sintered bodies were characterized by X-ray diffraction (XRD, Panalytical X'Pert ProMPD, Cu Kα radiation wavelength λ = 1.5405 Å, scan speed of $4^\circ\,min^{-1}$). The microstructures and the morphology of the prepared powders and sintered bodies were determined using a field emission–scanning electron microscope (FESEM, Hitachi Field-Emission S4800 (EMAX)). The average grain size was calculated from a series of micrographs by the linear-interception method. The Archimedes method was used to measure the sintered density. The sintered bodies were coated with a silver paste by firing. The electrode-coated samples were connected to Pt wires on the surface of both electrodes by clamping the wires in a spring – loaded sample holder. The samples with electrodes and Pt conduction wires in a holder were placed into a tube furnace to measure the conductivity and the impedance at temperatures in the range of 200–750 °C. The DC conductivities at the temperatures set, and with a holding time of 1 h in air were measured by four wire-probes using a Keithley 2400 source meter. The AC impedance measurement was carried out using an electrochemical instrument (Zahner Zennium, Germany) under an open circuit condition in the frequency range of 10 MHz–1.0 MHz. The Pt wires with insulating shield were connected to the cables with BNC connectors to reduce the induction effect. The AC impedance spectra generally showed depressed arcs due to non-ideal capacitance. Such a non-ideal capacitance can be described through a constant phase element (CPE). Thus, the measured impedance spectra were fitted with a built-in program of Zahner EIS measurement algorithm according to RQ equivalent circuits including parallel resistance/CPE circuits in series. In the RQ equivalent circuits, R represents a resistance and Q a constant phase element, which is characterized by two parameters, C_Q and n. Corresponding capacitances (C) can be calculated from $C = (R^{1-n}C_Q)^{1/n}$. The grain resistance (R_g) and capacitance (C_g), and the grain-boundary resistance (R_{gb}) and capacitance (C_{gb}) of the samples were obtained in this way.

3. Results and discussion

In order to evaluate the thermal reaction behavior of the powders, the SS- and SV-prepared powders were subjected to thermal analysis (TG/DTA) in air. For the SS-powders heated in air, the thermogravimetric loss (TG) was completed at a temperature above 1000 °C. For the SV-prepared powders, the moisture and the organics were completely decomposed by the time the temperature reached 400 °C (not shown). The result of the TG shows that the stable thermogravimetry, without weight loss for SS powders, heated

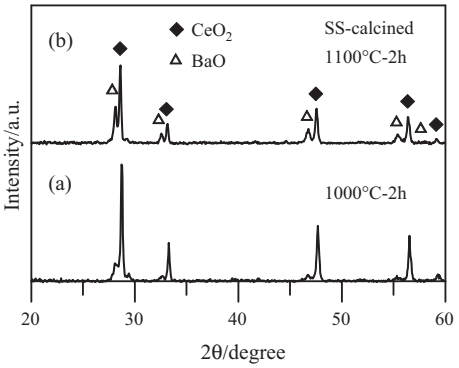

Fig. 1. XRD patterns of calcined SS powders, calcination at (a) 1000 °C–2 h, and (b) 1100 °C–2 h.

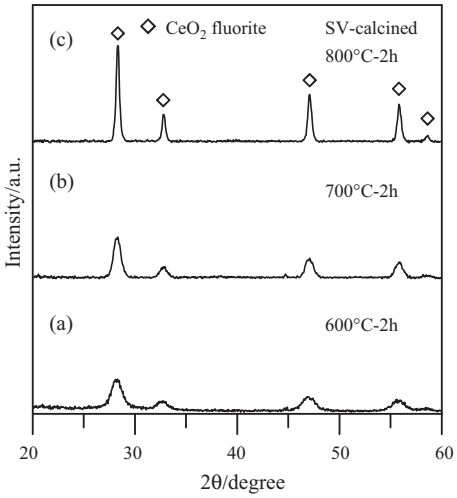

Fig. 2. XRD patterns of calcined SV powders, calcination at (a) 600 °C–2 h, (b) 700 °C–2 h, and (c) 800 °C–2 h.

up to more than 1000 °C, the crystal structure could not reach the pure phase of the ceria fluorite structure (JCPDS 34-0394) until 1100 °C–2 h calcination, as shown in Fig. 1. The second phase of barium oxide (BaO) (JCPDS 22-1056) remained accompanied with the fluorite lattice. This might be due to the fact that the ionic radius of Ba^{2+} is larger than that of Ce^{4+}. The insufficient solubility of BaO in ceria [9,11] at a calcined temperature resulted in the second phase, as shown in Fig. 1b.

The homogeneity of doped atoms in the electrolyte is a very serious problem. For example, the electrical conduction largely depends on the concentration distribution of rare earth elements in ceria [9]. The powder preparation method and the heat treatment process strongly influence the homogeneity and stability of the electrolyte solid solutions [10]. The pure phase of fluorite crystal can be obtained by calcining SV powders, as shown in Fig. 2. However, the crystallinity increases as well with the increased temperature of the calcined powders. The pure ceria fluorite structure occurs at a temperature as low as 600 °C (Fig. 2a). The development of crystallinity at heat-treating temperatures matches the results of TG/DTA. A well-crystallized phase without residual carbon was grown at 800 °C–2 h for SV prepared powders, as shown in Fig. 2c. The XRD analyses shown in Figs. 1 and 2 indicate that the SV samples exhibit a more homogeneous doping distribution than the SS samples, and behave more like a pure fluorite structure.

The morphology of typical SV powders after 800 °C–2 h calcination is shown in Fig. 3a. A homogeneous particle size of less than 50 nm is achieved. An agglomeration of powders is present among the as-calcined powders. Micron scale particles sizes and the agglomeration of powders in the calcined SS powders are shown in Fig. 3b. A comparison of Figs. 1–3 showing the two powder preparation methods, presents that well-crystallized nanoparticles of multiple doping solid electrolyte materials were successfully prepared by the SV method at a temperature as low as 600 °C.

High sintering temperatures are needed for the SS samples to facilitate the doped component of Ba into the fluorite lattice becoming a pure structure of ceria, as shown in Fig. 4a. This higher sintering temperature allows the development of the fluorite structure to become more complete without a second phase, referred to Fig. 1. When the SV powders are heat treated by conventional sintering (SV-CS), the fluorite structure is kept at 1400 °C–6 h, as shown in Fig. 4b. This comparison shows that SV nanoparticles have a better sinterability compared to solid-state (SS) reaction powders, also see the sintering density comparison of SS-CS and SV-CS, as per Table 1.

In this study, we attempted to lower the sintering temperature as well as shorten the time required to treat solid electrolyte LSBC, by using microwave sintering (MW). Microwave sintering is well-known to result in a short sintering time, a fast processing rate, being environmentally friendly as well as resulting in a homogeneous grained microstructure [31,32]. Both SS and SV disks were microwave sintered in the focused electromagnetic field of a microwave cavity designed by our group [31]. The SS samples were treated by microwave sintering at 1400 °C–15 min to develop crystallization similar to the SV samples conventionally sintered at 1400 °C–6 h, see Fig. 4b and c. The SV samples sintered by microwave at 1400 °C, were only sintered for 15 min (Fig. 4d). The SS samples sintered by conventional method to develop crystallization were sintered at a temperature above 1450 °C for 6 h, as shown in Fig. 4a. These results illustrate that the nanopowders and the microwave sintering process enhanced the lattice formation. Especially the microwave energy was dominant for the densification over a short treatment. The relative sintering den-

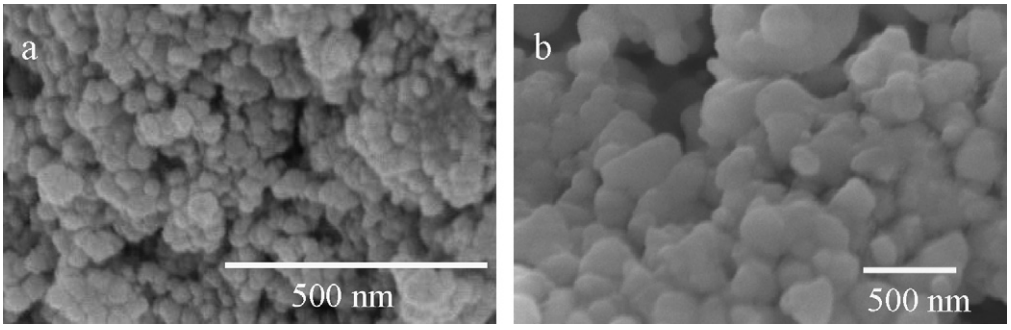

Fig. 3. FESEM images of typical (a) SV and (b) SS powders morphology of calcination.

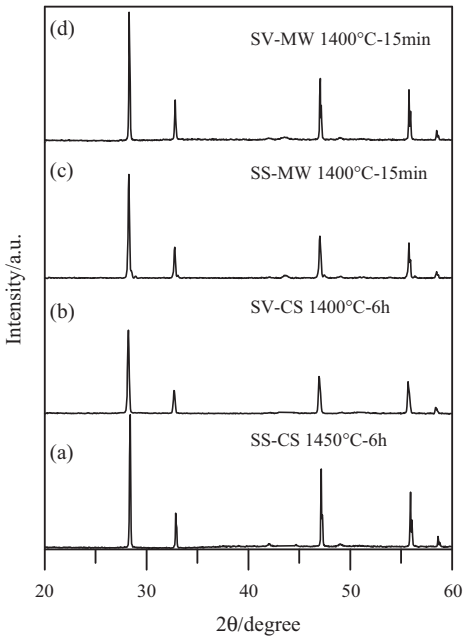

Fig. 4. XRD patterns of sintered samples of SS and SV powders, (a) SS conventional sintered (SS-CS) at 1450 °C–6 h, (b) SV conventional sintered (SV-CS) at 1400 °C–6 h, (c) SS microwave sintered (SS-MW) at 1400 °C–15 min and (d) SV microwave sintered (SV-MW) at 1400 °C–15 min.

sity and the grain size shown in Table 1 indicate that the result of SS-MW 1300 °C–15 min was comparable to SS-CS 1400 °C–6 h, and that the result of SS-MW 1400 °C–15 min was comparable to SS-CS 1500 °C–6 h.

The DC conductivities of the sintered bodies were measured by a Keithley 2400 source meter at 450–750 °C. The conductivity of conventional-sintered SS samples (SS-CS) for various sintering temperatures showed no difference in the range of intermediate operating temperature, 450–600 °C, as shown in Fig. 5a. The conductivities of 1300–1500 °C–6 h sintered SS-CS samples were all about 0.004 S cm^{-1} measured at 600 °C. Higher conductivities were obtained at higher sintering temperatures, with an operating temperature above 600 °C. This could be the reason for the higher densification and grain growth of higher sintering temperatures, see the inset micrographs in Fig. 6. In addition, the SS samples were sintered by microwave for a period of 15 min. When the equivalent temperature reached 1400 °C, the measured conductivity was far higher than for the 1200 °C and 1300 °C microwave-sintered samples. The conductivity of 1400 °C–15 min microwave-sintered SS samples (SS-MW) is about 0.006 S cm^{-1} measured at 600 °C, as shown in Fig. 5b. This is higher than the conductivity of SS-CS at 1500 °C–6 h measured at 600 °C, see Fig. 5a and b. At a temperature of 750 °C, the conductivity of 0.02 S cm^{-1} of the 1400 °C–15 min SS-MW sample was almost the same as that of the 1500 °C–6 h SS-CS sample, as shown in Fig. 5a, b and d.

Table 1
The activation energy of grain (E_g) and grain boundary (E_{gb}), the migration enthalpy (H_m) and formation enthalpy (H_a) about oxygen vacancies, and the grain size (G.S.) including relative sintering density in parentheses with the sintering temperatures 1300–1500 °C for SS-CS, SV-CS, SS-MW and SV-MW (1300 °C–6 h, 1400 °C–6 h and 1500 °C–6 h are for SS-CS and SV-CS samples. 1300 °C–15 min and 1400 °C–15 min are for SS-MW and SV-MW samples).

		1300 °C	1400 °C	1500 °C
SS-CS	E_g (eV)	0.87	0.81	0.84
	E_{gb} (eV)	0.94	0.90	0.90
	H_m (eV)	0.65	0.62	0.61
	H_a (eV)	0.97	0.90	0.90
	G.S. μm (density %)	1.8 (89)	3.5 (90)	4.5 (98)
SV-CS	E_g (eV)	0.80	0.80	0.78
	E_{gb} (eV)	1.03	0.99	1.02
	H_m (eV)	0.67	0.65	0.65
	H_a (eV)	0.85	0.87	0.86
	G.S. μm (density %)	1.5 (84)	2.5 (92)	4.5 (99)
SS-MW	E_g (eV)	0.75	0.77	
	E_{gb} (eV)	0.92	0.76	
	H_m (eV)	0.66	0.66	
	H_a (eV)	0.78	0.81	
	G.S. μm (density %)	2.9 (90)	5.0 (92)	
SV-MW	E_g (eV)	0.78	0.77	
	E_{gb} (eV)	0.82		
	H_m (eV)	0.66	0.67	
	H_a (eV)	0.81	0.82	
	G.S. μm (density %)	1.0 (93)	2.0 (95)	

The conventional sintered SV samples (SV-CS) show no difference in conductive behavior in the range of 450–750 °C, as shown in Fig. 5c. This means a good sinterability of SV-prepared nanoparticles. The SV-CS sample sintered at 1400 °C–6 h can obtain a higher conductivity, 0.006 S cm^{-1}, than the SS-CS sample sintered at 1400 °C–6 h measured at the temperature of 600 °C, as shown in Fig. 5a and c. This behavior is believed to be the result of a more homogeneous dopants distribution in SV-CS bodies than in SS-CS bodies at nearly the same grain size and density (see Table 1) to facilitate oxygen vacancy mobility. When microwave energy is used to sinter SS samples (SS-MW), only a 15 min soaking time will result in the same high conductivity as the SV conventionally sintered bodies for the same sintering temperature of 1400 °C for 6 h (SV-CS). In addition, it obtains the same conductivity as the SS conventionally sintered bodies at 1500 °C–6 h (SS-CS) at a temperature measuring between 450 and 750 °C, see Fig. 5d. It is worth noting that the SV samples microwave sintered at 1400 °C–15 min achieved a conductivity as high as 0.01 S cm^{-1} at 600 °C, as shown in Fig. 5d. This demonstrates a far higher conductivity than that of the SS-CS samples sintered at 1500 °C–6 h, of the SV-CS samples sintered at 1400 °C–6 h and of the SS-MW samples sintered at 1400 °C–15 min, although the latter three processes obtained the same conduction properties as shown in Fig. 5d. The rapid sintering of nanoparticles by microwave is believed to lead to an intermediate grain growth and a high densification rate in the SV-MW samples, as shown in Table 1.

Fleig et al. [33] and Waser and Hagenbeck et al. [34] studied a variety of applications, including sensors, grain boundary devices, solid oxide fuel cells and others, using the impedance spectrum (IS) method. They proposed defect chemistry at the grain boundary based on IS analysis related to microstructures, and the geometries of the grains and grain boundaries of the studied materials. Defect chemistry at the grain boundary is concerned with the double Schottky barrier. In a solid electrolyte, the impedance of the material is related to its microstructure, because grain boundaries have a substantial effect on the charge transport. Pérez-Coll and Mather [35] showed that the origin of the grain-boundary resistance is most likely attributable to the space-charge phenomena, as expected for the grain size in the range from ~120 nm to the micron scale. The grain size is larger than 1 μm at least in our report (see Table 1), thus the brick-layer model [33,34,36] is utilized. Bulk transport properties depend on the level of densification and composition homogeneity, whereas grain-boundary transport is also dependent on the grain size. This is reflected in a sharp decrease in grain-boundary resistance when densification reaches completion and grain growth becomes predominant, as shown in the curve of SS-CS 1500 °C–6 h in Fig. 6. The resistivity to oxygen ion conduction contains an intra-grain resistivity ρ_g and a grain-boundary resistivity ρ_{gb}. This total resistivity is represented as $\rho_0 = \rho_g + \rho_{gb}$ (or $R_0 = R_g + R_{gb}$) and can be distinguished in AC-impedance data, but not in a DC measurement. The R_g and R_{gb} are obtained from the interception on the axis of real impedance (Re Z) with RQ curve

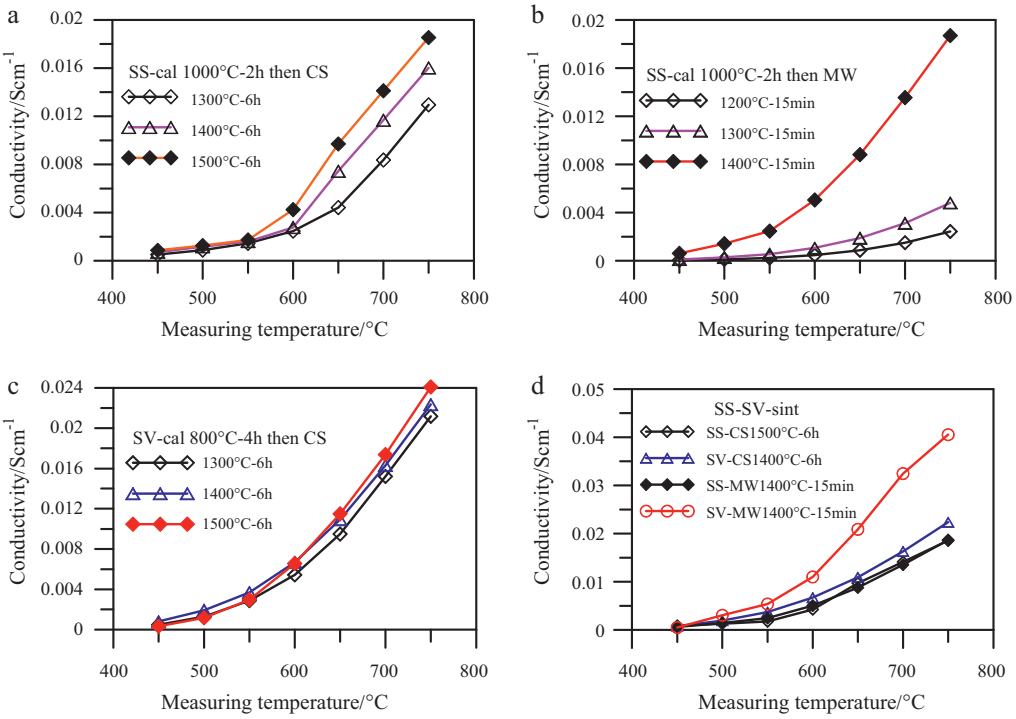

Fig. 5. DC conductivities as function of operating temperatures for different sintering conditions, (a) SS-CS, (b) SS-MW, (c) SV-CS and (d) comparisons of SS-CS, SS-MW, SV-CS and SV-MW samples.

fitting. A high R_{gb} can be due to many factors, including amorphous phases, dopant segregation, altered local defect chemistry due to space charge effects, and intergranular porosity. All these effects are strongly related to grain size and the associated grain-boundary area. Fig. 6 shows the effect of the grain-boundary on the decreasing resistance of SS-CS multi-doped ceria electrolyte with increasing grain size. On the other hand, the doping of rare-earth and alkaline-earth oxides into ceria considerably improves the ionic conductivity due to the formation of oxygen vacancies ($V_0^{\bullet\bullet}$), which are the charge carriers of oxide-ion conduction. The double Schottky barrier formed in the grain boundary regions are as a result of the depletion of oxygen vacancies. The Schottky barriers increase with the decrease in grain size. The increase in Schottky barriers increases the resistance due to the increase in grain boundaries [33,34,36]. The contribution of the grain boundary resistance in the impedance spectra shown in Fig. 6 therefore increases with the decrease of grain size like the 1300 °C–6 h SS-CS sample as shown in the inset micrograph. When the SS-CS sample is sintered at a higher temperature of 1500 °C–6 h, the fast grain growth reduced the number of grain boundaries and decreased the contribution of the grain boundary resistance, as shown in Fig. 6. However, the apparent resistance to oxygen vacancy mobility in grains remains largely unchanged for the sintering temperatures between 1300 °C and 1500 °C.

In accordance with the brick-layer model [33,34,36], for a positive space-charge potential, positive carriers, such as oxygen vacancies and electrons holes, are depleted, and negative carriers, such as electrons, are enhanced in grain boundaries. The double Schottky barrier is then built at grain boundary to exhibit the blocking of ions passing through. The grain boundary resistance appears to become negligible at high temperature and above a constant concentration of dopants. Then, the properties of grain boundaries in the electrolyte play an important role in the ionic conductivity, especially at low temperature. This is proven in the results of Fig. 6. Generally speaking, the activation energy for the grain-boundary conductivity is higher than that for the grain conductivity. The concentration of oxygen vacancies in the space-charge layer increases with the increase in temperature.

Zhou et al. [8] has shown the grain-boundary blocking effect disappeared at high enough temperatures, e.g., >600 °C. It is expected that completely free oxygen vacancies will exist at high enough temperatures. Zhou et al. [8] also showed that the contribution of grain boundary resistance of $Ce_{0.9}Gd_{0.1}O_{1.95}$ was eliminated at temperature >600 °C. The $Gd_{Ce'} - V_0^{\bullet\bullet}$ complexes dissociated at a critical temperature of ~580 °C. Similar results have been observed by Goodenough and colleagues [37] and Steele [16].

Fig. 7 shows that the grain-boundary blocking effect disappears gradually when the temperature increases from 300 °C to 600 °C, as shown by the 1400 °C–6 h SS-CS sample. The grain boundary resistance plays an important role at 300 °C. However, the small grain boundary resistance is almost covered by the electrode effect above 400 °C as shown in the inset figure of Fig. 7. The grain-boundary blocking effect disappears completely when the

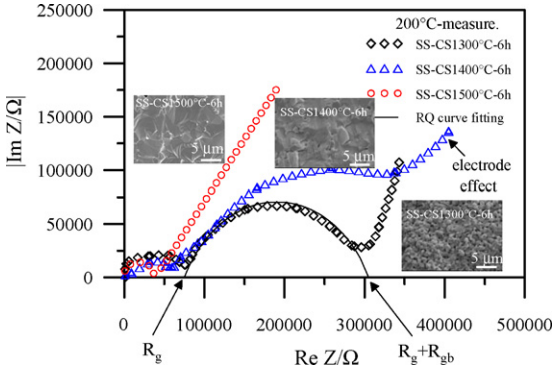

Fig. 6. AC impedance spectra of SS-CS samples sintered at 1300–1500 °C–6 h measured at 200 °C. The inset microstructures are FESEM micrographs of SS-CS samples sintered at 1300–1500 °C–6 h. The R_g and R_{gb} are obtained from the interception on axis of real impedance by RQ curve fitting.

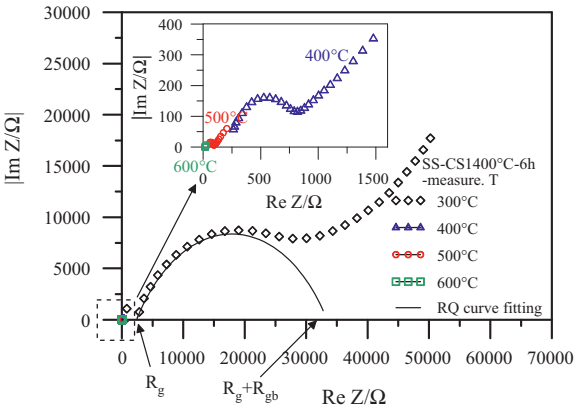

Fig. 7. Change of AC impedance spectra of SS-CS samples sintered at 1400 °C–6 h measured at 300 °C–600 °C. The inset figure is the enlargement of impedance spectra of 400, 500 and 600 °C.

temperature reaches 500 °C. This indicates that there is a possibility to use this electrolyte composition in the intermediate temperature of 500–600 °C.

The difference of average activation energy between grain (E_g) and grain boundary (E_{gb}) is about 0.1–0.02 eV calculated from 10 mol% Y_2O_3–CeO_2 by Guo et al. [38]. However, the difference of ($E_{gb} - E_g$) is larger than 0.1 eV for SV-CS, SS-MW and SV-MW samples except for SS-CS samples, as shown in Table 1. The double Schottky barrier height will decrease or disappear at sufficient high temperature. Then, the grain boundary blocking effect will disappear [33,34,38].

In order to confirm the R_{gb} location in the AC impedance spectra, different bias voltages were applied to the measured sample. Fig. 8a shows the 1400 °C–6 h SS-CS sample measured at 300 °C

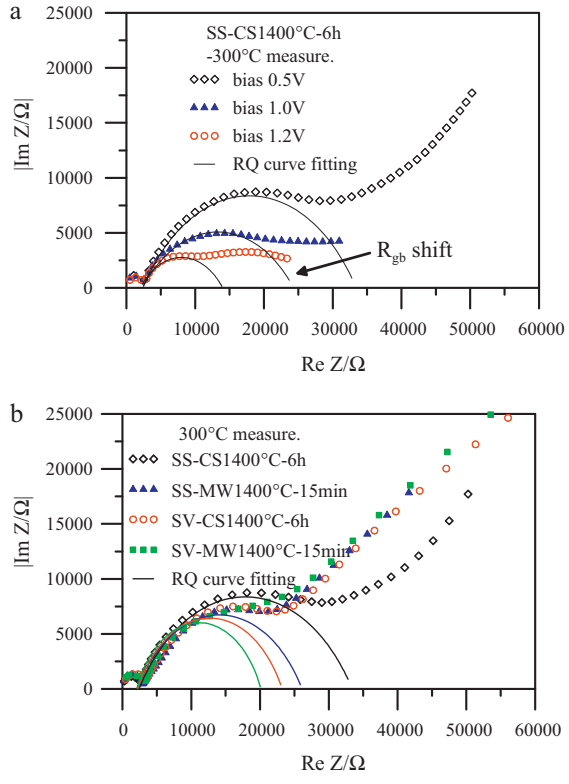

Fig. 8. AC impedance spectra of (a) SS-CS samples sintered at 1400 °C–6 h with different bias voltages, and (b) SS-CS, SS-MW, SV-CS and SV-MW samples sintered at 1400 °C for comparisons.

at different bias voltages of 0.5, 1.0 and 1.2 V. Generally, the grain properties are independent from the electrical field. The grain and grain boundary are then easily identified by applying the electrical field [39]. In other words, the grain boundary properties can be significantly changed by the DC bias due to oxygen vacancy depletion in the region shifting under bias direction. Fig. 8a indicates the R_{gb} location shift in the impedance spectra when the bias voltage increases. The location of the grain boundary part is then identified in the AC impedance plot by RQ curve fitting. The grain-boundary blocking effect disappearing completely, when the temperature is higher than 500 °C shown in Fig. 7, is identified by the bias.

Microwave sintering can refine the grain boundary effect for the conventionally sintered solid electrolyte of SS and SV samples, as shown by the reduction of grain boundary resistance in Fig. 8b and the reduction of E_{gb} in Table 1. Fig. 8b shows that the grain boundary resistance is reduced in the microwave sintering samples compared with both the SS-CS and SV-CS samples. The microwave process substantially modified the grain boundary properties resulting in a very short processing time for the same sintering temperature for both the SS-CS and SV-CS samples. To estimate the contribution of grain boundary resistance to the electrolyte conductivity, the ratio $R_{gb}/(R_g + R_{gb})$ was used to evaluate the grain boundary effect. The interception represents R_g and R_{gb} on the axis of Re Z, as shown in Fig. 8b is also by RQ curve fitting. In Fig. 8b, the R_{gb} contribution decreases for the SS-MW compared to the SS-CS samples. The R_{gb} contribution also decreases for the SV-MW compared to the SV-CS samples. The powder preparation method of SV and microwave sintering improved the grain boundary resistance reduction for SS-prepared electrolyte. The reason for the grain boundary resistance reduction by the microwave energy may be the possible elimination of amorphous phases and dopant segregation, as well as the reduction of local defects due to space charge effects. In addition, microwave energy homogenized the dopant distribution.

The oxygen vacancies for the ionic conductivity are due to the introduction of aliovalent ions by substituting Ce^{4+} in the ceria fluorite structure. The conductivities as a result of the large number of oxide ion vacancies generated from non-stoichiometry by doping may be altered by the charge carrier mobility that is affected by temperature. The ionic conductivity mechanism is due to the hopping of oxide ions to vacant sites and depends on the temperature being expressed by the following Arrhenius relationship [39]

$$\sigma T = \sigma_0 \exp\frac{-E}{kT} = \sigma_0 \exp\frac{-(H_m + H_a)}{kT} \quad (1)$$

where σ is the ionic conductivity, T is the absolute temperature, σ_0 is the pre-exponential constant, and E is the activation energy of the oxygen vacancies transport in the grains; H_m and H_a represent the enthalpy of free oxygen vacancies migration and enthalpy of formation of the ($R_{Ce'} - V_0^{\bullet\bullet}$) defect complexes, respectively, and R is the dopant.

There are three regions (I, II, and III) of the electrical conductivity dependent on temperature according to Kilner and Walters studies [40]. Since doped fluorite has a large number of oxygen vacancies and the electrical conduction is determined by extrinsic defects. There are only two regions exhibited in doped oxides. The region II is determined by an aliovalent dopant or impurity at higher temperature and the region III is determined by thermodynamic equilibrium between the free defects and the associated pairs at lower temperature. The mobility enthalpy (H_m) is considered to be independent of dopant, the variation of the activation energy with dopants can be ascribed to the association enthalpy (H_a). Therefore, the H_m can be obtained from region II and the H_a obtained from region III. Kilner and Walters mention that even the complex association energy ($H_a - H_m$) is small, the effects of association will manifest themselves as curvature in the conductivity vs. reciprocal temperature plots. This changeover from region III to

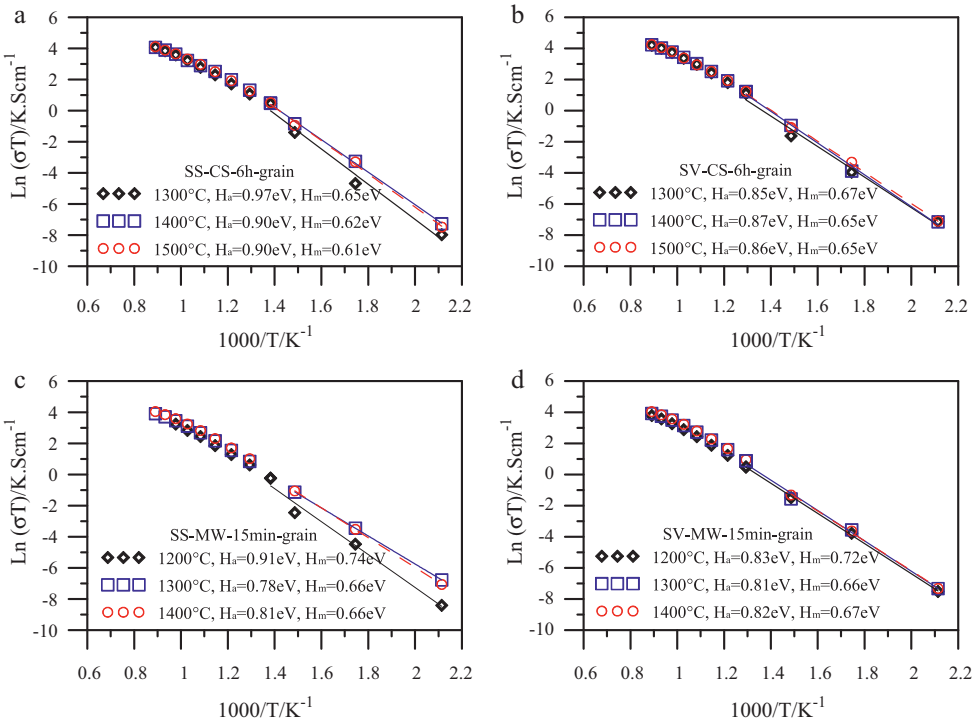

Fig. 9. Conductivity $\ln(\sigma T)$ as a function of $1000/T$ for calculation of formation enthalpy (H_a) and migration enthalpy (H_m) of oxygen vacancies for (a) SS-CS, (b) SV-CS, (c) SS-MW and (d) SV-MW samples.

region II type behavior is gradual [40]. The distinguished point of the changeover is thus determined by the intersection of the fitting lines between the higher and lower temperature data.

From Arrhenius plot, Steele showed the concentration of $[V_0^{\bullet\bullet}]$ is no longer independent temperature. In the curves of $\ln(\sigma T) - (1/T)$ experimentally, there are two regions at intermediate temperature that are a result from the extrinsic contribution due to the dopants [16]. The conductivity of the higher temperatures is controlled by the charge carrying defects determined by an aliovalent dopant or impurity. However, the conductivity of the lower temperatures represents the charge carrying defects determined by the thermodynamic equilibrium between the free defects ($V_0^{\bullet\bullet}$) and the associated pairs ($R_{Ce'} - V_0^{\bullet\bullet}$).

Therefore, the activation energy E normally includes energy terms for formation (H_a) and migration (H_m) of oxygen vacancies. Experimentally, the $\ln(\sigma T) - (1/T)$ relationship of the grains for SS-CS, SS-MW, SV-CS and SV-MW samples are indicated in Fig. 9. The grain conductivity is dependent on the temperature of two distinct regimes. It shows that the critical temperature of about 500 °C represents the dissociation of the acceptor-oxygen vacancy complexes [8]. This temperature shows that the SS-CS sample sintered at a temperature below 1500 °C with a high formation energy (H_a) for the associated oxygen vacancies by dopants below the 500 °C measurement, as shown in Fig. 9a. The associated pairs ($R_{Ce'} - V_0^{\bullet\bullet}$) dissociated above 500 °C in order to be free of defects ($V_0^{\bullet\bullet}$). The main role of overcoming activation energy H_m is to migrate the free oxygen vacancies. The migration enthalpy H_m is about 0.61 – 0.65 eV for the various sintered SS-CS samples in Fig. 9a. This seems to indicate that only the migration energy H_m is intimately related to the composition and crystallinity of the electrolyte.

The formation enthalpy (H_a) is not very different for SV-CS for different sintering temperatures, as shown in Fig. 9b. A homogeneous dopant distribution for the SV nanoparticles is considered to be associated with the oxygen vacancies. This finding can be confirmed by Fig. 5c. The formation enthalpy (H_a) ~0.81 eV for the SS-MW samples sintered at 1400 °C–15 min, and for the SV-MW samples sintered at 1300 °C–15 min and 1400 °C–15 min is also equal to ~0.81 eV, as shown in Fig. 9c and d. These results also indicate that the dopant distribution homogeneity is enhanced by microwave sintering. However, the crystallinity and composition dependent migration energy $H_m = 0.66 - 0.67$ eV were obtained by the SS-MW and SV-MW samples through 1400 °C–15 min sintering. This result is comparable with the high density and large-grained SS-CS sample sintered at 1500 °C–6 h, comparing H_m in Fig. 9a, c and d. This kind of behavior illustrates that the oxygen vacancy migration is independent from the sintering process but is dependent on composition and lattice development.

Microwave sintering in the short sintering time of 15 min reduced the sintering temperature and reduced the activation energy (resistance) of the grain boundary. This is evident if, for example, we compare SS-MW 1300 °C–15 min with SS-CS 1400 °C–6 h, and SS-MW 1400 °C–15 min with SS-CS 1500 °C–6 h, as shown in Table 1. In addition, a similar behavior also occurred in SV-MW 1300 °C–15 min with SV-CS 1400 °C–6 h, as shown in Table 1. Fig. 8b indicates the reduction of grain boundary resistance by microwave sintering more exactly. Furthermore, microwave sintering modified the grain boundary Schottky barrier to below 450 °C. As indicated in Table 1, the grain boundary resistance disappeared for the 1400 °C–15 min SV-MW sample in the AC impedance spectrum at 450 °C. This phenomenon illustrated that rapid sintering and the combination of nanoparticles can effectively reduce the grain boundary resistance, because the blocking and unblocking grain boundary effects depend greatly on homogeneous or heterogeneous materials. The formation of vacancies and excess electrons are easier in homogeneous media such as ceria [41]. This combination also homogenized the distribution of the dopants to increase the transport number of free oxygen vacancies, thereby enhancing the DC conductivity in the intermediate operating temperature, 600 °C, to over 0.01 S cm^{-1}. Therefore the Schottky barrier height can be adjusted by SV powder preparation and the microwave sintering process without raising the sintering temperature too high,

and with a short processing time for the multiple doping solid electrolyte.

4. Conclusion

The crystalline structure could not reach the pure phase of the ceria fluorite structure until 1100 °C–2 h calcination for the SS samples. A higher sintering temperature of 1500 °C was required to enhance the diffusion of the doping species into the fluorite structure for the SS samples. The pure ceria structure developed at a temperature as low as 600 °C for the SV powders. A homogeneous particle size of smaller than 50 nm was achieved after calcining the SV powders at 800 °C. The development of crystallization for the SS samples treated by microwave sintering (SS-MW) at 1400 °C–15 min was similar to the conventional sintering of the SV samples (SV-CS) at 1400 °C–6 h. The conductivity of SS-MW was about 0.006 S cm^{-1} measured at 600 °C. The SV samples microwave sintered at 1400 °C–15 min achieved a high conductivity of 0.01 S cm^{-1} measured at 600 °C.

The contribution of the grain boundaries resistance decreased with the increase in grain size for the 1300–1500 °C–6 h SS-CS samples. The grain-boundary blocking effect disappeared gradually with an increase in temperature, and then disappeared completely when the temperature reached above 500 °C. The grain properties were independent from the electrical field. The grain boundary properties can be changed by DC bias in order to identify the location of the grain boundary part in the AC impedance spectra. The microwave process substantially modified the grain boundary properties with the very short processing time. The R_{gb} decreased by use of microwave sintering for SS- and SV- samples, respectively. The grain conductivity showed a critical temperature of about 500 °C, representing the acceptor-oxygen vacancy complexes dissociation. The migration enthalpy H_m was about 0.61 – 0.67 eV for the various sintered samples. Microwave sintering over the very short sintering time of 15 min reduced both the sintering temperature and activation energy of the grain boundary. These results show that SS-MW 1300 °C–15 min is comparable to SS-CS 1400 °C–6 h, and SS-MW 1400 °C–15 min is comparable to SS-CS 1500 °C–6 h. Similarly, SV-MW 1300 °C–15 min is comparable to SV-CS 1400 °C–6 h. The microwave-sintering-modified grain boundary Schottky barrier was found to occur as low as 450 °C for the 1400 °C–15 min SV-MW sample. The grain boundary resistance disappeared for the 1400 °C–15 min SV-MW sample in the AC impedance spectrum at 450 °C. This phenomenon illustrated that rapid sintering and combination of nanoparticles can effectively reduce the grain boundary resistance.

Acknowledgements

The authors would like to thank the National Science Council, Taiwan, ROC and SGS Taiwan Ltd. for financially supporting this research under Grant No. NSC98-2622-E-019-005-CC3. The authors also acknowledge the funding support from Grant No. NTOU-RD982-01-04-12-01 of National Taiwan Ocean University and from Grant No. 9354DB2410 of Industrial Technology Research Institute, Taiwan, ROC.

References

[1] A. Atkinson, S. Barnett, R.J. Gorte, J.T.S. Irvine, A.J. McEvoy, M. Mogensen, S.C. Singhal, J.M. Vohs, Nat. Mater. 3 (2004) 17–27.
[2] D.J.L. Brett, A. Atkinson, N.P. Brandon, S.J. Skinner, Chem. Soc. Rev. 37 (2008) 1568–1578.
[3] M. Yashima, T. Takizawa, J. Phys. Chem. C 114 (2010) 2385–2392.
[4] T. Mori, J. Drennan, J.H. Lee, J.G. Li, T. Ikegami, Solid State Ionics 154–155 (2002) 461–466.
[5] Y.J. Leng, S.H. Chan, S.P. Jiang, K.A. Khor, Solid State Ionics 170 (2004) 9–15.
[6] N. Ai, Z. Lu, K. Chen, X. Huang, B. Wei, Y. Zhang, S. Li, X. Xin, X. Sha, W. Su, J. Power Sources 159 (2006) 637–640.
[7] S.Q. Hui, J. Roller, S. Yick, X.G. Zhang, C. Dec'es-Petit, Y.S. Xie, R. Maric, D. Ghosh, J. Power Sources 172 (2007) 493–502.
[8] X.D. Zhou, W. Huebner, I. Kosacki, H.U. Anderson, J. Am. Ceram. Soc. 85 (7) (2002) 1757–1762.
[9] H. Inaba, H. Tagawa, Solid State Ionics 83 (1996) 1–16.
[10] B. Matovic, Z. Dohcevic-Mitrovic, M. Radovic, Z. Brankovic, G. Brankovic, S. Boskovic, Z.V. Popovic, J. Power Sources 193 (2009) 146–149.
[11] K. Eguchi, T. Setoguchi, T. Inoue, H. Arai, Solid State Ionics 52 (1992) 165–172.
[12] J.V. Herle, T. Horita, T. Kawada, N. Sakai, H. Yokokawa, M. Dokiya, Solid State Ionics 86–88 (1996) 1255–1258.
[13] J.D. Nicholas, L.C. De Jonghe, Solid State Ionics 178 (19–20) (2007) 1187–1194.
[14] Y. Zhou, M.N. Rahaman, Acta Mater. 45 (1997) 3635–3639.
[15] J.K. Young, G.M. Choi, Solid State Ionics 180 (2009) 886–890.
[16] B.C.H. Steele, Solid State Ionics 129 (2000) 95–110.
[17] A. Atkinson, Solid State Ionics 95 (1997) 249–258.
[18] R.D. Purohit, S. Saha, A.K. Tyagi, Ceram. Int. 32 (2006) 143–146.
[19] P. Muralidharan, S.H. Jo, D.K. Kim, J. Am. Ceram. Soc. 91 (10) (2008) 3267–3274.
[20] J.M. Im, H.J. You, Y.S. Yoon, D.W. Shin, Ceram. Int. 34 (2008) 877–881.
[21] A. Heel, A. Vital, P. Holtappels, T. Graule, J. Electroceram. 22 (2009) 40–46.
[22] R.D. Purohit, B.P. Sharma, K.T. Pillai, A.K. Tyagi, Mater. Res. Bull. 36 (2001) 2711–2721.
[23] A. Bodén, J. Di, C. Lagergren, G. Lindbergh, C.Y. Wang, J. Power Sources 172 (2007) 520–529.
[24] V.V. Ivanov, V.R. Khrustov, Y.A. Kotov, A.I. Medvedev, A.M. Murzakaev, S.N. Shkerin, A.V. Nikonov, J. Eur. Ceram. Soc. 27 (2007) 1041–1046.
[25] D. Pérez-Coll, J.C. Ruiz-Morales, D. Marrero-López, P. Núñez, J.R. Frade, J. Alloys Compd. 467 (2009) 533–538.
[26] S. Dikmen, J. Alloys Compd. 491 (2010) 106–112.
[27] Z. Jiao, N. Shikazono, N. Kasagi, J. Power Sources 195 (2010) 151–154.
[28] R. Chockalingam, V.R.W. Amarakoon, H. Giesche, J. Eur. Ceram. Soc. 28 (2008) 959–963.
[29] B. Rambabu, S. Ghosh, W. Zhao, H. Jena, J. Power Sources 159 (2006) 21–28.
[30] B. Rambabu, S. Ghosh, H. Jena, J. Mater. Sci. 41 (2006) 7530–7536.
[31] H.Y. Chang, S.Y. Cheng, C.I. Sheu, Mater. Lett. 62 (2008) 3620–3622.
[32] S.N. Kale, J. Mona, S.E. Lofland, S.D. Kulkarni, S.B. Ogale, Appl. Phys. Lett. 92 (2008) 012512-1–112512-3.
[33] J. Fleig, S. Rodewald, J. Maier, Solid State Ionics 136–137 (2000) 905–911.
[34] R. Waser, R. Hagenbeck, Acta Mater. 48 (2000) 797–825.
[35] D. Pérez-Coll, G.C. Mather, Solid State Ionics 181 (2010) 20–26.
[36] X. Guo, R. Waser, Prog. Mater. Sci. 51 (2006) 151–210.
[37] K. Huang, M. Feng, J.H. Goodenough, J. Am. Ceram. Soc. 81 (1998) 357–362.
[38] X. Guo, W. Sigle, J. Maier, J. Am. Ceram. Soc. 86 (1) (2003) 77–87.
[39] H.L. Tuller, in: O.T. Sørensen (Ed.), Nonstoichiometric Oxides, Academic Press, New York, 1981.
[40] J.A. Kilner, C.D. Walters, Solid State Ionics 6 (1982) 253–259.
[41] J. Maier, Solid State Ionics 175 (2004) 7–12.